

3D WIND AND TURBULENCE CHARACTERISTICS OF THE ATMOSPHERIC BOUNDARY LAYER

BY R. J. BARTHELMIE, P. CRIPPA, H. WANG, C. M. SMITH, R. KRISHNAMURTHY, A. CHOUKULKAR, R. CALHOUN, D. VALYOU, P. MARZOCCA, D. MATTHIESEN, G. BROWN, AND S. C. PRYOR

The 3D Wind experiment integrates model simulations and measurements from remote-sensing, traditional, and unmanned aerial vehicle platforms to quantify wind components over the area of a large wind farm to heights of 200 m.

The 3D wind and turbulence characteristics of the atmospheric boundary layer experiment (3D Wind) focus on collection and integration of data from remote sensing and in situ instruments to develop precise and accurate characterization of wind and turbulence in the lowest 200 m of the atmospheric

boundary layer (ABL). This research is conducted within the context of applications to wind resource characterization, wind farm optimization (design and operation), and wind farm aerodynamics for power production and fatigue load quantification. These end uses require data over a range of temporal (and spatial) scales from individual turbines (seconds–minutes) through wind farms (minutes–hours) and clusters of wind farms (hours–days and onto years) (Fig. 1). Scales responsible for dynamic and fatigue loads on individual turbine blades are related to the average turbulence intensity (defined as the standard deviation of wind speed divided by mean wind speed over a time interval) and thus are a function of length scales from centimeters to hundreds of meters. In contrast, a 200-MW wind farm comprising approximately 130 wind turbines (with rated capacity of 1.5 MW typical of those currently found in much of the Midwest) would occupy an area of about 8 km by 8 km (~15,000 acres), assuming an even turbine spacing in the south–north and west–east directions of eight rotor diameters.

Given the limitations in terms of spatial coverage of data from instrumentation deployed on fixed meteorological masts, the emergence of ground-based remote sensing technologies, including vertically pointing and scanning light detection and ranging

AFFILIATIONS: BARTHELMIE, CRIPPA, WANG, SMITH, AND PRYOR—Atmospheric Science Program, Department of Geological Sciences, Indiana University, Bloomington, Indiana; KRISHNAMURTHY, CHOUKULKAR, AND CALHOUN—Environmental Remote Sensing Group, Arizona State University, Tempe, Arizona; VALYOU AND MARZOCCA—Mechanical and Aeronautical Engineering, Clarkson University, Potsdam, New York; MATTHIESEN—Case Western Reserve University, Department of Material Science and Engineering, Cleveland, Ohio; BROWN—SgurrEnergy Ltd., Vancouver, Canada

CORRESPONDING AUTHOR: Rebecca J. Barthelmie, Ph.D., Professor, Atmospheric Science and Sustainability, Department of Geological Sciences, Multidisciplinary Science Building II, 702 N Walnut Grove, Indiana University, Bloomington, IN 47405
Email: rbarthel@indiana.edu

The abstract for this article can be found in this issue, following the table of contents.

DOI:10.1175/BAMS-D-12-00111.1

In final form 9 July 2013

©2014 American Meteorological Society

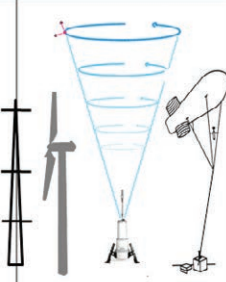
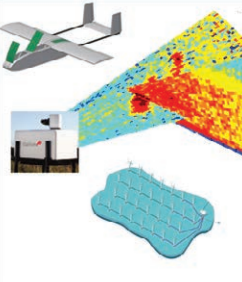
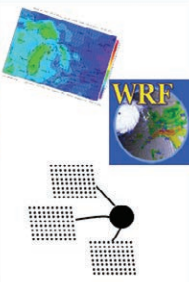
Space-scales	Local/ wind turbine 100's m	Regional/ wind farm 10's km	Mesoscale/ wind farm clusters 100's km
			
Time-scales	←Seconds-minutes	Minutes-hours	Hours-days→

FIG. 1. Schematic of the experimental design showing the spatial and temporal scales that are of importance to wind farm design and operation and the tools deployed to characterize wind conditions on those scales.

instruments (lidars), offers tremendous opportunities for improved understanding of the ABL. Potential applications within the wind energy industry include wind speed and turbulence characterization for resource estimation and siting (Gottschall et al. 2012; Koch et al. 2012; Krishnamurthy et al. 2012) and for wake characterization studies (Barthelmie et al. 2013, 2010; Hirth et al. 2012; Lungo et al. 2013; Kocer et al. 2011; Newsom et al. 2012), provided they can be demonstrated to exhibit performance in terms of precision and accuracy comparable to research grade anemometry (Clive 2012; Gottschall et al. 2012; Mann et al. 2009). Evaluation of these measurement tools, strategies to integrate measurements from disparate instruments and models across these time and space scales, and applications to characterized near-surface wind conditions are described here.

EXPERIMENTAL SITE AND INSTRUMENTATION. *Experimental site.* The measurement and analysis techniques developed within this project will be deployed for offshore wind characterization, but the initial experiment described herein was undertaken at a wind farm in northern Indiana (7–20 May 2012, inclusive). The instrumentation deployed is described in detail below and summarized in Table 1. Confidentiality agreements preclude full disclosure of the experimental location but, as shown in the schematic in Fig. 2, the majority of instruments were deployed in the southwest (SW) corner of the wind farm close to a 80-m meteorological mast (MM) displaced 170 and 200 m from the two nearest wind turbines. The fetch to the west, south, and east of the primary measurement site is typical of northern Indiana, comprising agricultural fields with very

few topographic features or buildings. The corn crop surrounding the MM was less than 10 cm in height, giving an approximate roughness length z_0 of about 0.05 m. There are no significant roughness changes for at least 4 km in all directions. An additional component of the experiment was the testing and evaluation of independent power supplies sufficient to allow autonomous offshore deployment. This was achieved using a battery bank and solar panel for all instruments except the Galion scanning lidar (Galion) for which the additional power requirements were met with a propane fuel cell. A “pre-experiment” phase

of approximately 1 month (4 April–7 May 2012) confirmed that the power quality from the combined solar panel–battery backup readily met the needs for all instrumentation including the vertically pointing continuous wave lidars (ZephIRs). An unmanned aerial vehicle (UAV, see sidebar) and tethersonde were operated from a private airfield 3 km south of the main site. Finally, a single ZephIR with power supply was located next to a MM 19.5 km to the northeast (NE) of the primary instrument site to provide free-stream wind characteristics (i.e., flow undisturbed by the wind farm) when the wind direction was from the north sectors. All measurements are reported in eastern standard time (EST).

Instrumentation. **ANEMOMETERS ON METEOROLOGICAL MASTS.** The two 80-m MM are purpose built with classic triangular tapering lattice structure and identical instrumentation deployed on long booms (tapering from 3 m at the top of the MM to 5.5 m at the lowest height) extending east and west (see Table 1 and Fig. 2). At 80 m, booms are oriented to the west and east. Wind speeds presented herein were selected from the anemometer in the free stream to reduce mast interference effects. Data availability for both the experiment and preexperiment phase is 100% for wind speeds at the three heights used herein (Fig. 3).

VERTICALLY POINTING CONTINUOUS WAVE LIDARS (ZEPHIR). Natural Power’s ZephIR uses a continuous wave laser at an eye-safe wavelength of 1.55 μm . This version of the instrument measures at five preselected heights between 20 and 200 m. The beam is focused at the specified height using a rotating prism and reports an average wind speed, turbulence intensity, and wind

direction at that height based on three scans of 1 s, each representing one complete rotation of the prism (Smith et al. 2006). Given that the wind speed at each height is determined from about 50 measurements of the radial velocity on the azimuth circle (from the

Doppler shift in radiation backscatter from atmospheric aerosols) (Sathe et al. 2011), the calculated wind speed is not sensitive to one or two anomalous returns that are screened by the software. However, the beam is inclined at 15° from the vertical, giving

UNMANNED AERIAL VEHICLE (UAV)

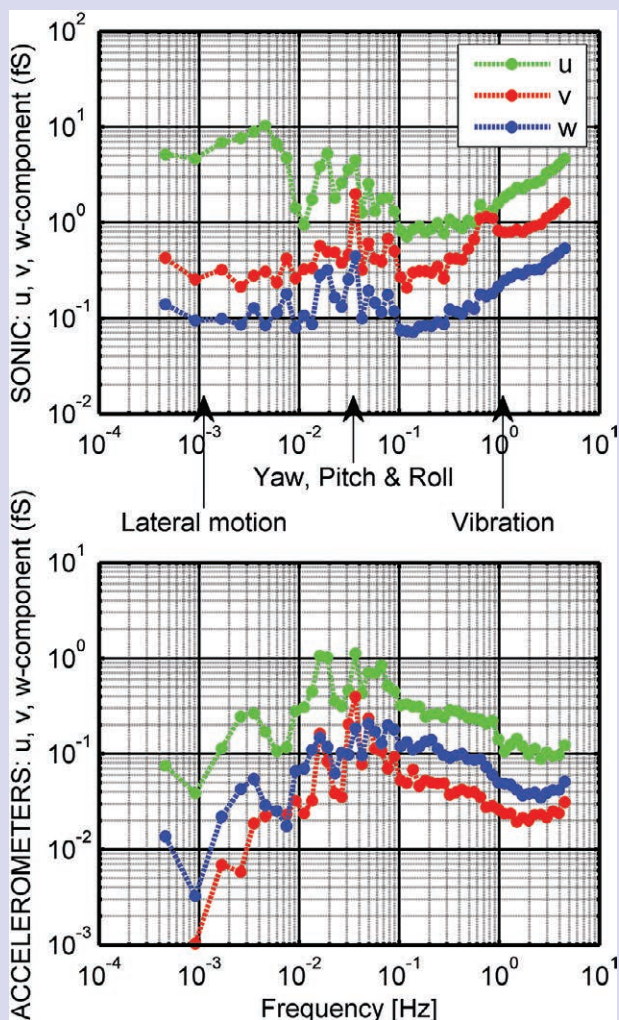
The Golden Eagle UAV has a 2.8-m wingspan, a pusher propeller configuration, and an empty weight of 18.1 kg. The cruise speed is 33.5 m s⁻¹, and the takeoff and landing speed is 20.1 m s⁻¹. Only 150 m of runway is needed for operations. The UAV was equipped with a 3D ultrasonic anemometer (Table 1), which was tested and calibrated in a high-speed wind tunnel. In the 3D Wind experiment, nine data collection flights were carried out with 20–30-min average flight times. Data collected included relative wind velocity components as well as aircraft pressure altitude, airspeed, components of acceleration, GPS location, heading, and ground speed, along with flight control system performance data. Application of sonic anemometers on mobile platforms for wind and turbulence measurements requires correction of the wind velocity components (*u*, *v*, and *w*) measured in a fixed-reference frame with respect to the platform for movement of that platform (Lenschow 1986). As shown in the example given below, the frequencies associated with (i) platform lateral motion, (ii) yaw, pitch, and roll, and (iii) vibration are readily identifiable in sonic



FIG. SB1 (ABOVE). The crew for the field experiment and the UAV “Golden Eagle” with mounted sonic anemometer.

FIG. SB2 (RIGHT). (top) Power spectra of the two horizontal components (*u* and *v*) and the vertical wind component (*w*) (all in m² s⁻²) as measured by the UAV-mounted sonic on one flight during 17 May. (bottom) Power spectra (m² s⁻⁴) of the accelerometer data. The frequencies associated principally with variations in the lateral speed of the UAV, the yaw, pitch, and roll of the UAV, and the vibration of the sonic anemometer on the boom extending from the nose of the UAV are indicated by the vertical arrows.

signals for the three components. Corrections to remove this noise using data from the onboard accelerometers are nontrivial and introduce relatively large uncertainty into the absolute values of the resulting measurements. Nevertheless, as shown in Fig. 4, data processing for the 17 May flights is complete and has yielded wind speeds that exhibit some degree of accord with wind speed measurements at 40, 80, and 120 m from the other instruments. To improve the accuracy of measurements, a custom attitude and heading reference system (AHRS) is being developed that combines microelectromechanical systems (MEMS) gyros and accelerometers with GPS data and a magnetic compass to accurately define the aircraft’s flight data.



a scan radius of 10.4 m at 40-m height increasing to 51.8 m at 200-m height, which limits the effective height range to about 200 m. The three ZephIRs used in the experiment are of the same generation and were operated to provide measurements of wind speed and turbulence intensity at five heights: 40, 80, 120, 160, and 200 m to match measurements on the MM and capture conditions across the turbine rotor plane (extending from 40 to 120 m). Data availability for each ZephIR was at least 95%, excluding periods

when the ZephIR at the SW MM was unavailable because it was moved (Fig. 3).

SCANNING PULSED LIDAR (GALION). The Galion from Sgurr Energy also employs a wavelength of 1.5 μm and measures the Doppler shift to determine wind characteristics but, in contrast to the ZephIR, uses a pulsed signal, which enables exact determination of the time-of-flight distance of the pulse (Sathe and Mann 2012). The Galion has a pulse repetition frequency of

TABLE 1. Location and specification of instrumentation/platform (H = measurement height, N is the range of the measured parameter, A is accuracy, R is the resolution, and U is the uncertainty).

Platform/ instrumentation	Owner	Measured parameters	Specifications
Meteorological mast wind sensor P2546	Wind farm operator	Wind speed	$H = 80.0$ m, $N = 0.4\text{--}70$ m s^{-1} ; distance constant 1.81 m
NRG40		Wind speed	$H = 60.8/41.5$ m, $N = 1\text{--}96$ m s^{-1} , $U = 0.14\text{--}0.45$ m s^{-1} at 10 m s^{-1} ; distance constant 2.55 m
MetOne 020C-I and NRG200P		Direction	$H = 76.0$ m, $N = 0^\circ\text{--}360^\circ$, linearity < 1%
MetOne 083E-I-35		Temperature and humidity	$H = 76$ m, $N = -50^\circ$ to $+50^\circ\text{C}$, $A = 0.1^\circ\text{C}$, $N = 0\%\text{--}100\%$, $A = \pm 2\%$
MetOne 064-2		Temperature	$H = 2.5$ m
MetOne 090D		Pressure	$H = 76.0$ m, $A = 0.1$ hPa, $N = 600\text{--}1100$ hPa, $R = \pm 1.0$ hPa over full N
Natural Power ZephIR lidar (3)	Indiana University ($\times 2$), Case Western Reserve University (1)	u , v , and w components of wind speed, direction, turbulence	$H = 10\text{--}200$ m, wind speed $A = 0.5\%$
SgurrEnergy Galion lidar	SgurrEnergy	Wind speed	Range resolution 30 m, radial distance = 80–4000 m
Anasphere tethersonde ST5.0M, ST3.0G, ST3.0S, ST30B-15	Indiana University	Wind speed	$R = 0.1$ m s^{-1} , $A = 1$ m s^{-1} (or 5%), $N = 0\text{--}59$ m s^{-1}
		Wind direction	$R = 1^\circ$, $A = 2^\circ$
		Temperature	$R = 0.125^\circ\text{C}$, $A = 0.5^\circ\text{C}$, $N = -55$ to $+125^\circ\text{C}$
		Relative humidity	$R = 0.1\%$, $A = 3\%$, $N = 0\%\text{--}100\%$
Applied Technologies Inc. SATI-3A	Clarkson University	Pressure	$R = 0.1$ hPa, $A = 0.5$ hPa, $N = 0\text{--}1100$ hPa
		Wind speed	$R = 0.01$ m s^{-1} , $A = 0.01$ m s^{-1} , $N = \pm 65$ m s^{-1}
		Wind direction	$R = 0.1^\circ$, $A = 0.1^\circ$
Eagle Tree Systems Pro Recorder	Clarkson University	Temperature	$R = 0.01^\circ\text{C}$, $A = 2^\circ\text{C}$, $N = -50$ to $+60^\circ\text{C}$
		Aircraft speed	Airspeed: 1 m s^{-1} , GPS speed: 0.1 m s^{-1}
		Altitude	Pressure: $A = 0.3$ m, GPS: $A = 5$ m
		Position	$A = 2.5$ m
		Heading	$A = 0.2^\circ$

20,000 Hz averaging 10,000–15,000 pulses to produce “beams” of data every 3 s. For this experiment, the range-gate length (distance between two radial measurements) was set at 30 m, and the scan definitions were set such that the azimuthal spacing between

beam products was 3° or less. The horizontal resolution [based on a plan position indicator (PPI) scan with an angle from the horizontal of 3°] between two successive beam measurements is approximately 4 m at the first range gate (i.e., 30 m from the Galion) to

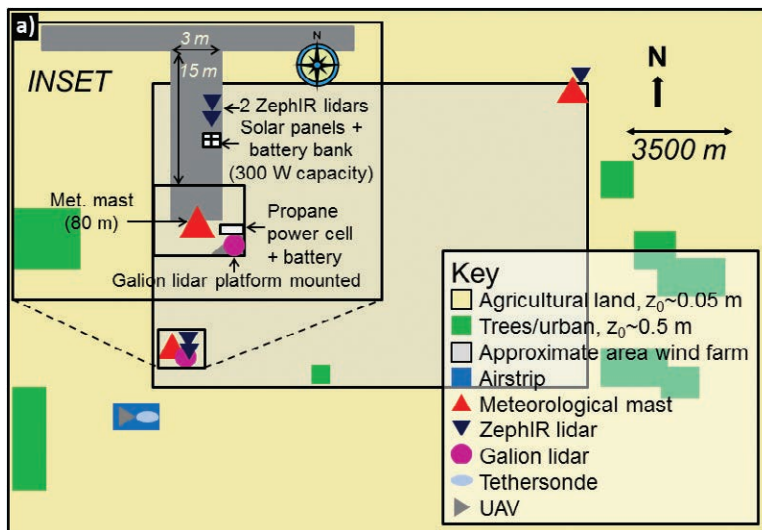


FIG. 2. (a) Schematic of the measurement location. The underlying map shows the approximate dimensions of the wind farm (and the roughness length z_0) and the relative locations of the three sites at which instruments were deployed: a private airstrip about 3 km to the SW of the wind farm, the primary experimental site on the SW corner of the wind farm, and the site at the NE of the wind farm. The inset in the upper left shows detail of the instrument location at the primary site (at the MM in the SW corner). (b),(c) Photos of the instruments as deployed at the SW MM.

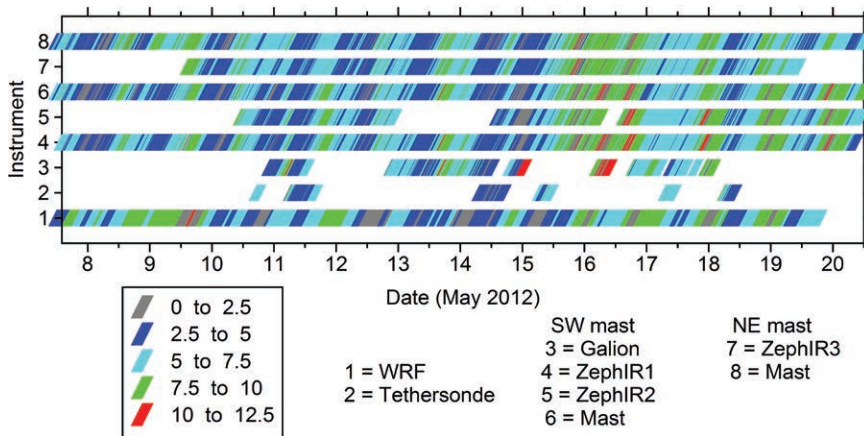


FIG. 3. Availability and magnitude of 10-min-mean wind speeds from the different instruments and WRF simulations during the experimental period. The colored bar indicates the wind speed at 80-m height (m s^{-1}). The different rows show the instruments from which measurements are presented, so, for example, the row denoted “4” indicates wind speeds from the ZephIR located at the SW MM.

approximately 105 m at the farthest range gate used for this analysis (because of the diverging beams). The scan definitions were selected such that the vertical resolution between successive elevation angles was about 34 m at the farthest range gate. The accuracy of the radial velocity is about 0.1 m s^{-1} , while the accuracy of the horizontal wind speed is a nonlinear function of the alignment of the beam relative to the prevailing wind direction and the extent to which the flow within the probe volume is homogeneous. A variety of signal processing approaches can be used to derive horizontal wind speed measurements from radial wind velocities (e.g., Choukulkar et al. 2012; Krishnamurthy et al. 2012; Pichugina et al. 2008). In brief, the approach adopted here applies a signal-to-noise threshold of 1.01 to identify a robust Doppler shift and determines the horizontal wind speed using a sine fit to the radial component (e.g., Matejka and Srivastava 1991). To calculate the average wind speeds presented at the MM, five or more observations had to be within 500 m of the MM x or y coordinate, within ± 10 m of the height stated, between 1 and 40 m s^{-1} , and have a standard deviation of less than 3 m s^{-1} . Three scan types were used during the experiment, in part to evaluate their performance and utility under different atmospheric conditions: PPI, range–height indicator (RHI), and velocity–azimuth display (VAD). Combined PPI–VAD scan configurations were used 52% of the time and the remainder as VAD profiles 25%, PPI scans for comparison with other instruments or capture wind turbine wakes 15% and RHI scans of wakes 8%. Instrument availability was high, but in order to provide a consistent basis

for cross comparison with the other measurements only wind speeds derived from the PPI scans are presented herein, limiting the number of observations available for the cross comparisons (Fig. 3). The main reasons for focusing on the PPI scans here are that the RHI scans can really only be utilized when the scanning direction and wind direction are aligned and the VAD profiles do not provide the necessary spatial information. Further information relating to the use of lidar in wind energy meteorology is given in

Banta et al. (2013) and Gottschall et al. (2012).

TETHERSONDE. Tethersondes are useful for monitoring wind and temperature profiles but are rather labor intensive for ongoing measurements (Högström 1988). An AnaspHERE tether sonde with a 4.6-m blimp and two instrument modules for measuring pressure, temperature, relative humidity, wind speed, and wind direction with a maximum data reporting frequency of 1 s was operated from a private airstrip (Table 1; Fig. 2). Operation was limited to daylight hours and to a maximum height of 500 ft (~ 152 m) by the Federal Aviation Authority regulations (note these limits are location specific), but over the course of the experiment about 30 h of measurements were taken (Fig. 3). To provide coherence with the other measurements the two sondes were placed on the tetherline about 40 m apart and operated sequentially at three heights (40 and 80 m, 80 and 120 m, and 120 and 160 m) for 10-min periods, except during early morning when a scanning pattern tracing the profile from 5 to 200 m was used to provide detailed data on the vertical wind shear during ABL destabilization.

WRF simulations. Numerical simulations of the ABL from the Weather Research and Forecasting Model (WRF) (Skamarock and Klemp 2008) were included in the study. WRF was run with 50 vertical levels in a nested grid with lateral boundary conditions from the North American Mesoscale Model. The outer grid has 324×274 cells of 9-km resolution (covering almost the entire eastern United States), while the inner nested grid (which was centered on the wind farm)

was 310×259 grid cells of 3 km. The physics options selected include the Rapid Radiative Transfer Model and the Mellor–Yamada–Janjic planetary boundary layer (PBL) scheme. The U.S. Geological Survey (USGS) 24-category land use data at 3.7-km resolution was used for the parent domain and at 0.9 km for the inner domain. The land use is homogenous over the wind farm area; each grid cell is classified as dryland, cropland, or pasture. In the following, wind speeds were extracted for the bottom three layers at 28, 97, and 192 m. Simulated wind speeds at 97 m were interpolated to 80 m for comparison with the measurement datasets using correction factors derived from the stability-corrected logarithmic wind profile applied with $z_0 = 0.05$ m and an hourly estimate of the Monin–Obukhov length (Stull 1988). In the WRF simulations, no local data assimilation was used, no postprocessing calibrations were applied, and no bias correction was undertaken; thus, the model output can be treated as truly independent of the observations. Parameterization of the wind farm (e.g., Fitch et al. 2012) was not included in the WRF simulations that are designed to describe ABL behavior in the absence of the wind farm.

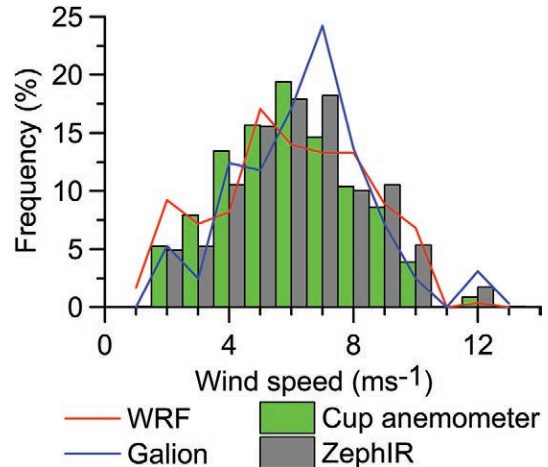
RESULTS. *Instrument intercomparison.* All the instruments deployed during 3D Wind have unique characteristics and advantages and disadvantages. Instruments and platforms designed to operate continuously and remotely such as the lidars and anemometers deployed on MM have high data availability over the experiment period (Fig. 3). The UAV and tethersonde have lower availability due to obvious constraints such as restrictions precluding launching in darkness or in wind speeds of at least 7 m s^{-1} close to the ground or during gusty or high wind shear events. However, these mobile platforms offer the possibility of wind speed measurements above traditional MM heights (to about 1 km assuming relevant permission can be obtained) and can readily be moved. To facilitate integration, the main height for intercomparison of measurements was 80 m corresponding to the turbine hub height, with additional levels (when available) of 40 and 120 m to span the rotor plane and 160 and 200 m to provide additional comparison between measurements from the UAV, tethersonde, and lidars to WRF simulations. The Galion and WRF are critical to quantifying the spatial variability of wind speed over all or part of the wind farm and the Galion bridges the spatial scales extending from the MM and ZephIR point measurements toward the larger scales simulated with WRF. The ZephIRs are insensitive to data degradation due to the angle of attack of the

wind relative to the beam direction, and they provide profiles of both wind speed and turbulence intensity to 200 m with relatively little data postprocessing. However, the Galion can scan to greater heights and WRF can provide output for numerous vertical levels. Integrating these disparate data streams is challenging, but the synthesis provides unique insights into the 3D characteristics of the boundary layer and an opportunity to assess optimal strategies for both measurements and modeling.

Figure 3 shows an overview of the degree of agreement between wind speed measurements and output from WRF, and generally indicates qualitatively good agreement with a few exceptions such as the higher wind speeds from the Galion during 16 May. To provide a more quantitative assessment, two metrics were computed for each instrument combination. The Pearson correlation coefficient r is used as a measure of the linear association (i.e., covariability), while the slope and intercept of a regression equation show the degree of bias (from the intercept) and proportionality of response for a linear change in wind speed (from the slope). The results indicate that r is highest for the collocated (Galion and ZephIR) lidars and the anemometers on the MMs (see Table 2). Time-averaged wind speeds measured by the cup anemometers and lidars on opposite sides of the wind farm are also highly correlated, validating use of this site as a suitable testbed location for the instrument intercomparison due to the relatively modest spatial variability in flow conditions. Correlation coefficients for the Galion and the measurements from the other continuously operated instruments are greater than 0.8, although the sample size of coincident observations is limited due to the variable scanning strategy used, which was designed to facilitate analyses of wind speeds retrieved from the different scan geometries. The high degree of agreement in 10-min-averaged wind speeds between collocated lidars and MM-mounted anemometers is in accord with a similar intercomparison conducted in Denmark that found that for a forced zero intercept the regression line for data from a sonic anemometer and a ZephIR had a slope of 0.99 (Sathe et al. 2011). In a further comparison correlation coefficients of 0.95 were obtained between wind speeds and directions from scanning lidars and cup anemometer measurements (Krishnamurthy et al. 2012), while wind speed measurements from ZephIR and cup anemometers in flat terrain gave correlation coefficients between 0.99 and 1.00, depending on atmospheric stability (Sanz Rodrigo et al. 2013). The ZephIR deployed at the NE MM appears to have a

TABLE 2. Comparisons of 10-min-mean wind speeds at 80 m. In each cell the top line shows the Pearson correlation coefficient (boldface). The second and third lines in each cell show results for regression fits ($y = mx + c$), where y is the wind speed time series from the instrument shown by the rows, and x denotes the time series from the instrument shown in each column. Thus, the regression coefficients shown are the intercept c (italics) and the slope m (normal text). The bottom value in each cell shows the number of 10-min observations available for the analysis. Note that the sample size (number of observations) shown has not been corrected for temporal autocorrelation. If the grid cell has solid gray shading, then the correlation coefficient is not significant at the 95% level. The wind speeds from the WRF simulation are for the closest grid cell to the SW MM corrected to 80-m height from 97 m as described in the main text. Cells for which the metrics are shown in red with no box shading indicate the instruments/measurements were displaced in space by more than 3 km; if the text is blue with vertical gray shading, then the instruments were displaced by 3 km or less; and if the text is shown in black with horizontal gray shading the instruments/measurements were collocated. Note that the Galion-derived wind speeds include returns from within 500 m of SW MM. The embedded figure shows the probability distribution of 10-min-mean wind speeds from all instruments/measurements and WRF simulations for SW MM. Data are included from both NW MM and SW MM.

Correlation coefficient <i>Intercept ($m s^{-1}$)</i> Slope # of obs	Cup anemometer SW MM	Cup anemometer NE MM	ZephIR 1 SW MM	ZephIR 2 SW MM	ZephIR 3 NE MM	WRF SW grid cell	Galion SW MM
Cup anemometer NE MM	0.99 <i>-0.02</i> 1.03 #1,264						
ZephIR 1 SW MM	0.94 <i>0.59</i> 0.94 #1150	0.95 <i>0.60</i> 0.91 #1150					
ZephIR 2 SW MM	0.94 <i>0.84</i> 0.89 #677	0.95 <i>0.93</i> 0.85 #727	1.00 <i>0.37</i> 0.94 #854				
ZephIR 3 NE MM	0.83 <i>2.08</i> 0.69 #1,043	0.83 <i>2.15</i> 0.66 #1043	0.85 <i>1.79</i> 0.70 #1,065	0.83 <i>1.62</i> 0.73 #860			
WRF SW grid cell	0.36 <i>3.47</i> 0.38 #222	0.36 <i>3.55</i> 0.37 #226	0.44 <i>2.61</i> 0.48 #204	0.59 <i>0.98</i> 0.72 #119	0.51 <i>1.43</i> 0.67 #191		
Galion SW MM	0.89 <i>0.67</i> 0.93 #218	0.90 <i>0.79</i> 0.88 #218	0.91 <i>0.42</i> 0.93 #219	0.82 <i>0.46</i> 0.93 #65	0.79 <i>0.37</i> 0.96 #201	0.22 <i>4.99</i> 0.25 #220	
Tethersonde Airstrip	0.81 <i>0.77</i> 0.81 #145	0.80 <i>1.19</i> 0.68 #146	0.80 <i>0.57</i> 0.81 #142	0.79 <i>0.47</i> 0.82 #243	0.69 <i>0.78</i> 0.80 #134	0.11 <i>4.03</i> 0.10 #150	0.77 <i>2.02</i> 0.44 #31



calibration issue (identified as the large intercept value) that is evident in this comparison. All correlations are significant at the 95% confidence level except between the measurements from the Galion and the tethersonde versus WRF-simulated wind speeds for the grid cell containing the SW MM. The sample sizes for these comparisons are substantially lower than for the other comparisons, and the low correlation may be linked to the tethersonde flights occurring during the early morning hours when both vertical and spatial gradients of wind speed were largest (see below). However, results from the tethersonde-borne anemometers and measured wind speeds from the MM-mounted anemometers and the lidars are good. The regression fits for the collocated lidars and cup anemometers at the SW MM indicate low intercepts ($<1 \text{ m s}^{-1}$) and slope values of 0.9–1 indicating good agreement across the range of observed wind speeds (Table 2). Results from WRF indicate a large intercept and small slope that may be partially attributable to comparison of once hourly output from WRF at the model time step of 20-s- versus 10-min-averaged observations, but more likely reflect issues related to the ABL parameterization or the land use/land cover dataset employed.

Characterization of wind shear: A case study from 17 May 2012. A key aspect of both power production and loading on wind turbines is shear across the area swept by the rotor (Wagner et al. 2011). Thus, an analysis was undertaken of 17 May when the SW MM was predominantly in the free stream (i.e., not impacted by the wake of the wind farm because the wind direction was southerly). This was to determine the consistency of wind speeds at the five heights sampled by the ZephIR lidars, and hence the wind shear across the lowest 200 m of the ABL (Fig. 4). Early in the day the wind was from the northeast veering south after the passage of a weak cold front (Fig. 4). Wind directions measured by the ZephIR wind vane on the SW MM and simulated by WRF are consistent except during the breakdown of the nocturnal boundary layer. Wind directions from the ZephIR and WRF also show wind veering with height during the nocturnal hours. From midnight until 0400 local standard time (LST), the measurements at the SW site were in a direct turbine wake, and thus all of the observed wind speeds at the wind turbine hub height (i.e., in the wind turbine wake center) were lower than those simulated by WRF. The Galion also exhibited higher wind speeds than the mast-mounted cup anemometers likely due to the spatial sampling, which meant it was not as strongly impacted by the

presence of wind turbines upstream (see the section below that discusses a wake study). However, it is noteworthy that wind speeds derived from the radial velocity estimates that are in turn derived from the Doppler shift were occasionally characterized by very high values likely due to a failure of the data analysis screening procedure to exclude false or erroneous returns. After 0800–0900 EST, the measurements at the SW MM were no longer impacted by wind turbine wakes. Subsequently 10-min-average wind speeds at 40 m measured by all instruments varied between about 4 and 8 m s^{-1} , and the standard deviation of measurements within each 10-min period from all instruments was relatively small and of consistent magnitude. Wind shear across the rotor plane was also consistent across the instrument suite, and wind speeds of 120, 160, and 200 m indicate exceptionally good agreement between the two types of lidar, the tethersonde, and output from the WRF simulations. Over the course of the entire field experiment, WRF wind speeds were generally negatively biased relative to the observations (Table 2). However, on 17 May the only major differences between WRF-simulated wind speeds and the measured wind speeds occur during the breakdown of the nocturnal boundary layer that appeared on this day to be delayed in the WRF simulations relative to the observations. Higher wind speeds persisted aloft in the WRF simulations after the ZephIR, and Galion data suggested a decrease caused by enhanced vertical mixing had commenced. Similar results in terms of delays in atmospheric stability transitions as modeled in WRF were noted by Storm et al. (2009).

Characterizing spatial gradients of wind speed: A case study of 18 May 2012. Even in this flat terrain with homogeneous land cover, important spatial gradients of wind speed were observed particularly over the nighttime and during the breakdown of the nocturnal boundary layer. Figure 5 shows an example of these gradients as simulated by WRF and measured by the ZephIRs and cup anemometers during 18 May. Wind speeds at 80 m were high overnight and the WRF simulations indicate a strong gradient from southeast to northwest. The spatial gradients and the discrepancies between measured data and output from WRF were large during the early morning (up to 2.5 m s^{-1} gradient over the modeled area shown—a distance of about 25 km) but were greatly reduced during the deeply convective conditions that prevailed during the afternoon. Measured and simulated wind speed profiles indicate the stable nocturnal boundary layer with relatively high wind shear began to destabilize at

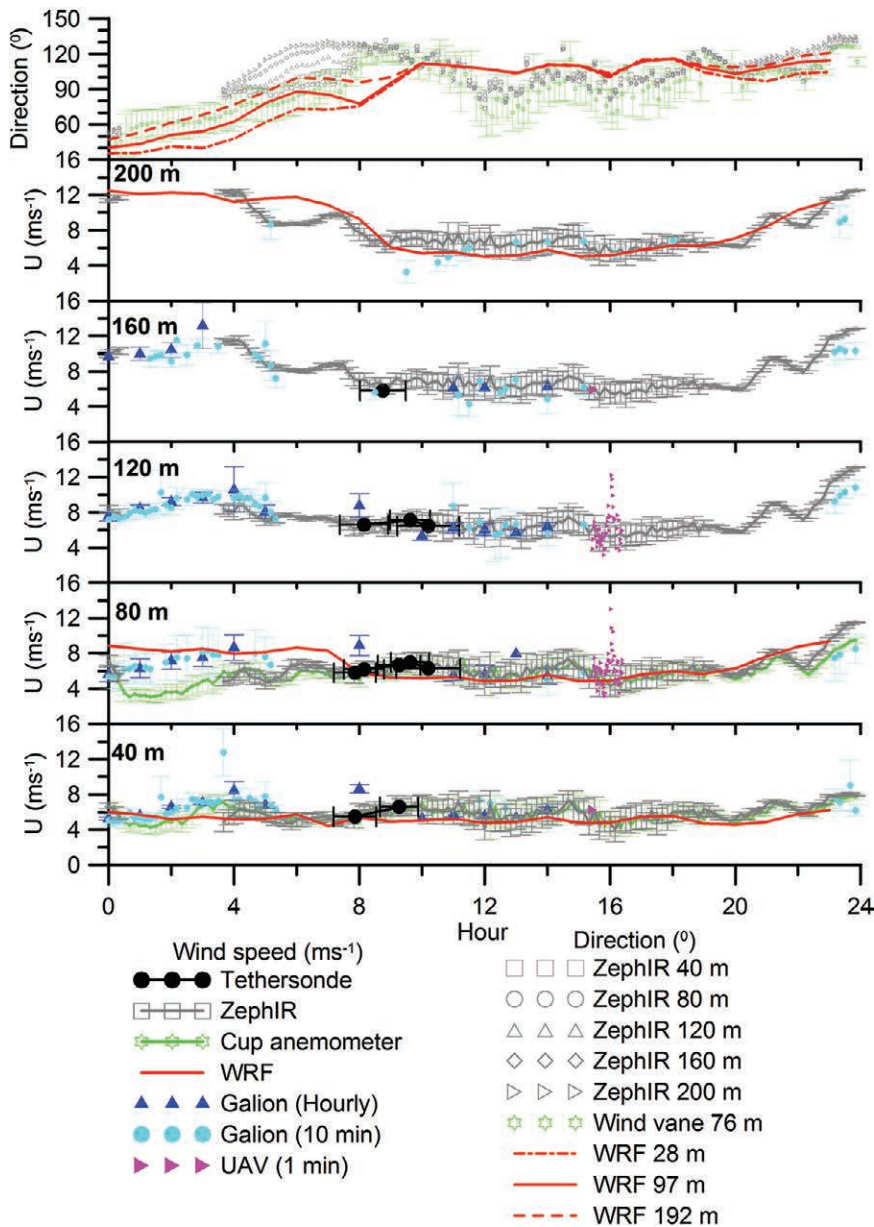


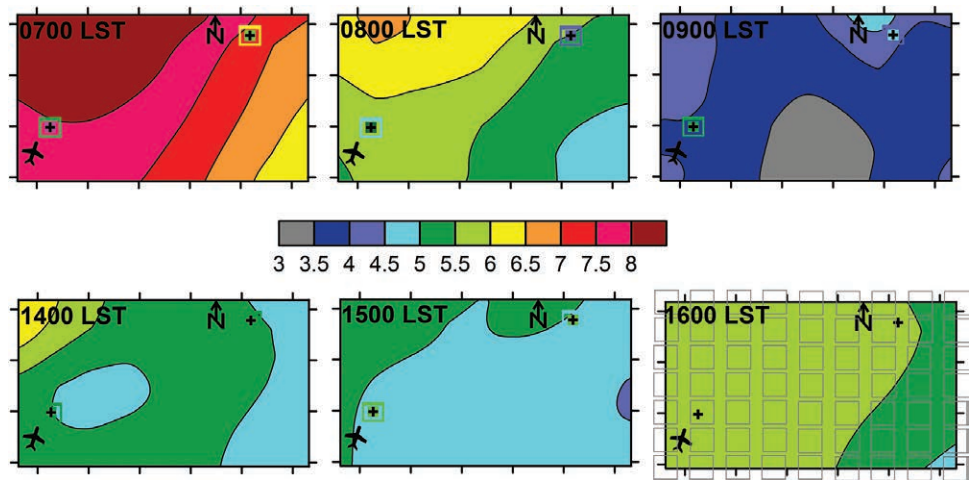
FIG. 4. Time series of wind speeds measured or simulated at different heights during 17 May 2012. Note the WRF output is for heights of 192, 97, and 28 m, and wind speeds have been vertically interpolated to the heights shown as described in the text, but the wind directions have not been modified and are for the heights indicated in the legend. The wind speeds from the tethered sonde are for the measurement height noted ± 10 m. Error bars for all measurements denote ± 1 standard deviation around the mean for the 10-min period. Data from the Galion are presented for individual 10-min periods and as hourly averages. Note that for a Galion wind speed to be reported, there must be more than 20 valid data points within each 10-min period and that data from the Galion represent a mean of data collected over a horizontal area of about $500 \text{ m} \times 500 \text{ m}$. Data from the UAV are 1-min-average wind speeds within ± 20 m of the specific height. Data are shown from one ZephIR at the SW site. (top) Wind direction is measured at the wind vane on the SW meteorological mast at 76 m (with ± 1 standard deviation shown as error bars around the mean), from the ZephIR at the SW site for heights shown between 40 and 200 m, and from WRF for heights of 28, 97, and 192 m.

approximately 0800 EST (Fig. 6) and transitioned to be characterized by lower wind speeds, lower wind shear, and higher turbulence intensity (Fig. 6) that persisted into the afternoon. As indicated by the measurement error bars shown in Fig. 6, all measured and modeled wind speeds are within one standard deviation of each other, except during the transition period from stable conditions overnight to unstable conditions during the daytime.

Wind turbine wake characterization: A case study from 14 May 2012.

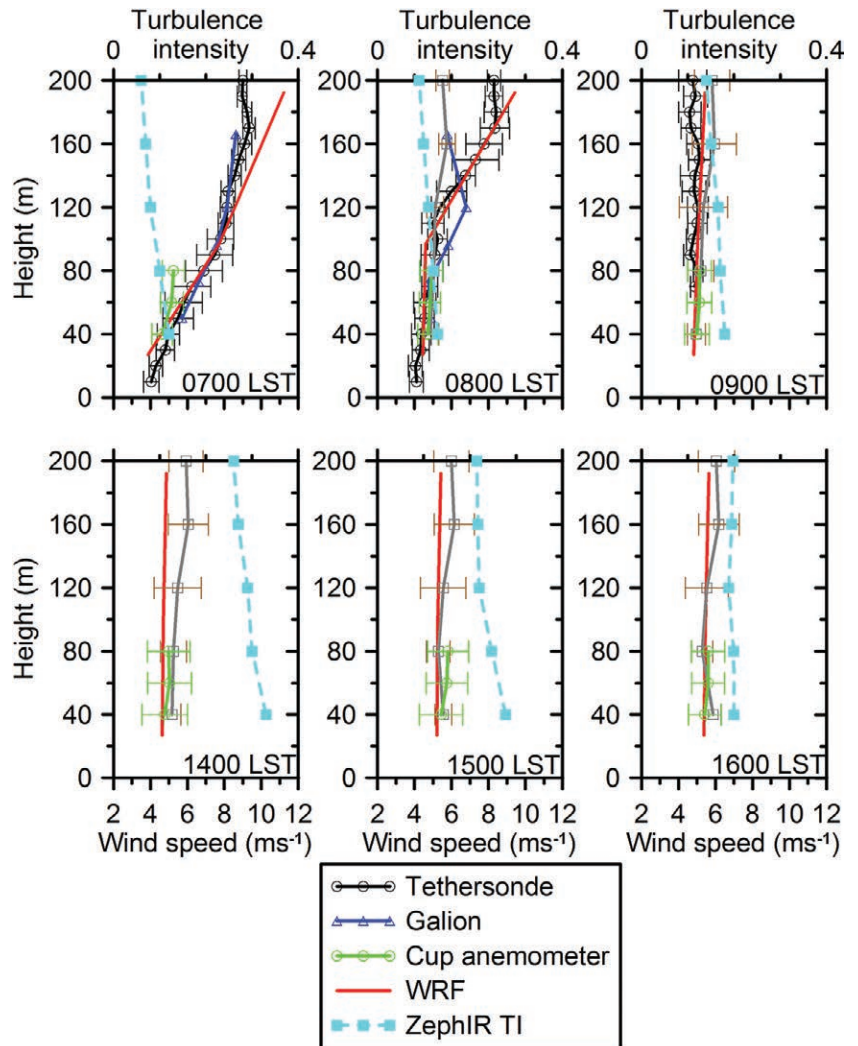
There is a need for observational data to support the development and evaluation of wind turbine wake models (Barthelmie and Pryor 2013; Sande et al. 2011). An example of wind turbine wakes as depicted on PPI scans from the Galion is shown in Fig. 7, together with plots where those data have been analyzed to produce constant elevation horizontal slices. These data were collected when the Galion was scanning downwind of the wind farm and sampled wind turbine wakes from the three closest upstream wind turbines. Consistent with expectations, the wind turbine wakes are most evident at hub height (80 m); at a downstream distance of approximately $7D$ (D is the wind turbine blade diameter) for this 20-min period, the average wake wind speed U_{wake} was about 5.4 m s^{-1} . The 80-m wind speed incident upon the upstream wind turbine derived from the two ZephIRs is 6.7 m s^{-1} , while that from the anemometer on the MM is 6.9 m s^{-1} , and the value estimated from unwaked regions sampled by the Galion is about 6.5 m s^{-1} . The free-stream

FIG. 5. Wind speed (m s^{-1}) at 80 m AGL during 18 May 2012 as simulated by WRF and measured by the ZephIRs and on the MMs (crosses) deployed in the SW and NE corners of the wind farm (separated by a distance of 19.5 km). The airplane symbol marks the location of the airfield, and the tick marks on both axes show a distance equivalent to 0.05°



(~ 5500 m for latitude and ~ 4300 m for longitude). The contours show wind speeds from WRF, while hourly average wind speeds from anemometers on the two MMs are shown by the outer squares, and data from the collocated lidars are shown by the inner filled squares. If the symbol appears not to be present, the measured wind speed from that instrument agrees with that from WRF to within the resolution of the wind speed bin (i.e., they agree to within $\pm 0.5 \text{ m s}^{-1}$). The grid in the bottom-right graph shows the WRF simulation grid from which the contours were generated.

FIG. 6. Hourly average wind speed profiles for 0700–0900 EST, inclusive, and 1400–1600 EST 18 May 2012. The error bars on each measurement denote are ± 1 standard deviation around the mean. The wind speeds from the scanning lidar shown in Fig. 6 were derived for a distance of about 1.3-km south of the MM and were processed using the technique described in Krishnamurthy et al. (2012). These measurements were thus almost coincident in space with the tethersonde and exhibit relative good agreement with cup anemometers deployed on the tethersonde.



wind speed $U_{\text{freestream}}$ is therefore in the range $6.5\text{--}6.9 \text{ m s}^{-1}$. Thus, the wake magnitude at this downwind distance (expressed as $U_{\text{wake}}/U_{\text{freestream}}$) was $0.78\text{--}0.83$ (where the range shows the variation in free-stream values). Employing the Wind Atlas Analysis and Application Program (WAsP) Park wake model (Barthelmie et al. 2009), a wake-decay coefficient of 0.075 and a thrust coefficient of 0.8 indicate the wake wind speed is

86% of the free-stream value. Thus, wake wind speed estimates from the WASP Park model are in relatively good agreement with those derived from the Galion data and are certainly within the uncertainty bounds of the assumptions employed in this calculation. Note that the WASP Park model uses a top-hat depiction of the wake and indicates a wake width at this distance of 160 m that is approximately 3 times the pixelization of the data shown in Fig. 7.

SUMMARY AND PROSPECTS. The 3D Wind experiment was designed to evaluate innovative remote sensing and in situ platforms for measurements of wind and turbulence regimes in the lowest 200 m of the ABL. Results from this experiment show that

both types of lidars exhibit very close agreement with collocated cup anemometers at heights extending across the rotor plane of the current generation wind turbines (i.e., Pearson correlation coefficient $r \geq 0.89$ and a high degree of linearity in response to varying wind speed). Data from cup anemometers deployed on a tethered balloon also exhibited $r \geq 0.8$ with the closest lidars and MM-mounted cup anemometers. Thus, while there remain some discrepancies between wind speed datasets from these instruments, the degree of accord is sufficient to remain cautiously optimistic.

Datasets deriving from experiments such as the one described herein offer a range of opportunities for exploring fundamental questions pertaining

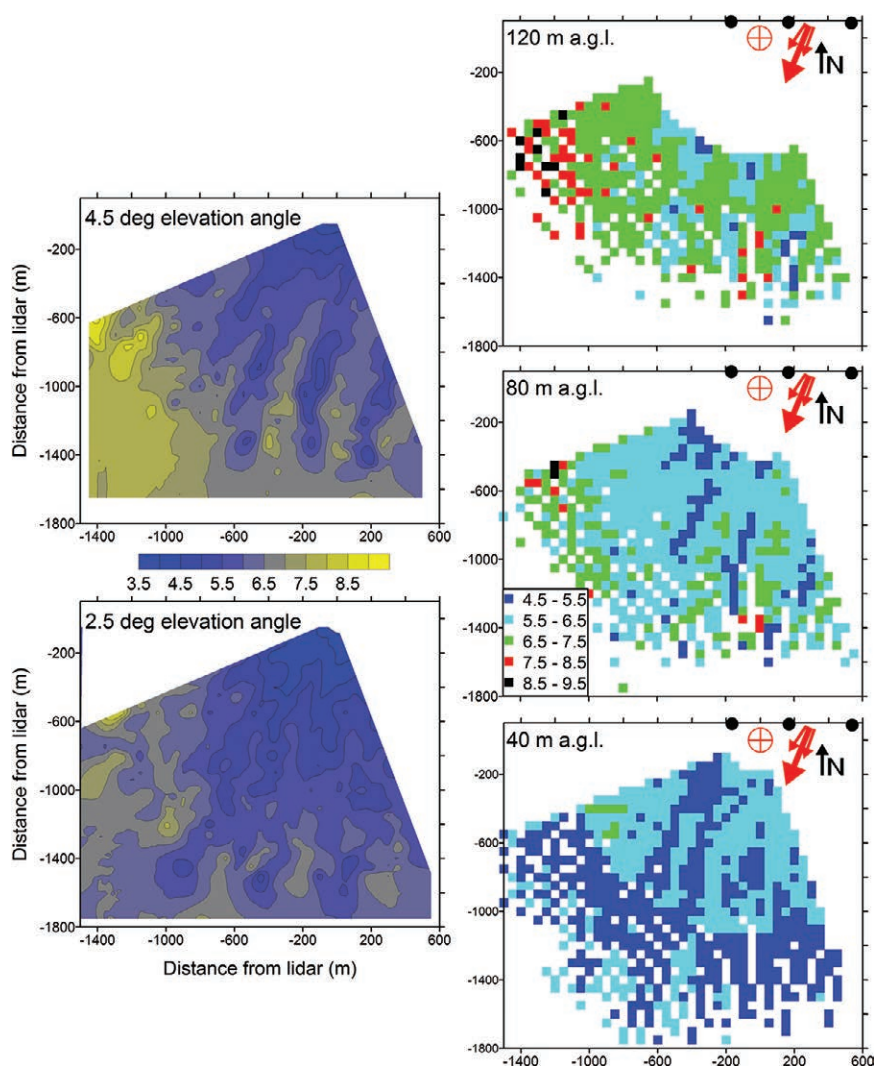


FIG. 7. Case study of wind turbine wakes using data the Galion collected during 2003–2023 EST 14 May 2012. The Galion scan configuration was designed to sample azimuth angles of 160° – 250° , at elevation angles of 1.5° – 8.5° , and data were only deemed valid if the signal-to-noise threshold of 1.01 was exceeded. During this period the wind direction was 14° – 30° ; thus, the Galion was scanning directly downstream of nearby wind turbines. (left) Direct output from constant elevation scans at (bottom) 2.5° and (top) 4.5° from the horizontal, where the horizontal wind speed (m s^{-1} ; derived from the Doppler shift) is shown by the color bar. (right) Constant elevation plots at (top) 120 m (at the rotor tip), (middle) 80 m (hub height), and (bottom) 40 m AGL (at the lower rotor tip), where the horizontal wind speeds (m s^{-1} ; determined from the radial velocity) is as denoted by the legend shown in the middle panel. These constant-elevation scans are based on resampling of PPI data from the eight scan angles and in

each the pixel size is $50 \text{ m} \times 50 \text{ m}$ (horizontal scale), and a pixel is only populated if more than 10 valid data points exist within $\pm 10 \text{ m}$ for 40 m AGL, $\pm 20 \text{ m}$ for 80 m AGL, and within $\pm 30 \text{ m}$ for 120 m AGL. Thus, white regions on all figures indicate missing data or unsampled areas. The red circumscribed plus signs show the location of the Galion, the black dots show the relative locations of the closest wind turbines, and the red arrows depict the wind direction (dominant arrow) and the range of wind directions during this 20-min period.

to wind regimes within 200 m of the surface. For example, the degree of agreement between wind speeds as simulated by WRF in a 3 km × 3 km grid cell containing the primary measurement site indicates that for these simulations (using the Mellor–Yamada–Janjic PBL scheme and the USGS land cover classification), the destabilization of the nocturnal stable layer was delayed in WRF relative to the observations, leading to decreased correlation. Further, wind speeds at 80 m as simulated with WRF were, on average, lower than the measurements. This finding is consistent with results from previous applications to the marine PBL (Suselj and Sood 2010) but is in contrast to comparison conducted relative to wind profilers in Japan, which found a positive bias throughout the lowest 1000 m for all PBL schemes tested within WRF (Shimada et al. 2011). The WRF simulations presented herein were conducted primarily to examine spatial gradients of wind speed over the wind farm that were not related to wind turbine wakes. If the intent was evaluation of WRF, then a modeling design optimized to include more vertical layers in the boundary layer and matching of observational measurement heights and more frequent output of WRF-simulated wind speeds and possibly an additional (higher resolution) nest over the wind farm area should be employed.

Gradients of wind speed across the wind farm as simulated using WRF and measured using the instrument suite appear to be more pronounced at night. During the day the wind field was more homogenous, consistent with higher turbulence intensity and a more well-mixed ABL. Understanding these spatial gradients is key to both short-term forecasting of wind power production (Lange and Focken 2006) and modeling wind turbine wake losses from the entire wind farm (Barthelmie et al. 2010). Wind farms now comprise dozens or even hundreds of wind turbines, and thus very few turbines experience undisturbed inflow: there is a need for improved prognostic models of wind turbine wakes to improve layout design to maximized power production and minimize turbine fatigue loading. As shown by the case study presented herein, data such as that collected during 3D Wind and other campaigns such as the Crop Wind Exchange Experiment (CWEX) (Rajewski et al. 2013) offer opportunities both to improve understanding of wake dynamics and to undertake uniquely detailed field evaluation of current and future generation wake models.

Data analysis from the 2012 3D Wind experiment is ongoing, but initial results are very promising. “Lessons learned” with regard to instrument

operation and data analysis were integrated into a 2013 Lake Erie experiment.

ACKNOWLEDGMENTS. The authors gratefully acknowledge comments of three reviewers, the two land-owners and owners of the private airstrip, and Midwest Portable Power, LLC. This material is based upon work supported by the National Science Foundation (Awards 1067007 & 0723054) and the Department of Energy (Award Number DE-EE0005379). Disclaimer: This report was prepared as an account of work sponsored by an agency of the United States government. Neither the United States government nor any agency thereof, nor any of their employees, makes any warranty, express or implied, or assumes any legal liability or responsibility for the accuracy, completeness, or usefulness of any information, apparatus, product, or process disclosed, or represents that its use would not infringe privately owned rights. Reference herein to any specific commercial product, process, or service by trade name, trademark, manufacturer, or otherwise does not necessarily constitute or imply its endorsement, recommendation, or favoring by the United States government or any agency thereof. The views and opinions of authors expressed herein do not necessarily state or reflect those of the United States government or any agency thereof.

REFERENCES

- Banta, R. M., Y. L. Pichugina, N. D. Kelley, R. M. Hardesty, and W. A. Brewer, 2013: Wind energy meteorology: Insight into wind properties in the turbine-rotor layer of the atmosphere from high-resolution Doppler lidar. *Bull. Amer. Meteor. Soc.*, **94**, 883–902.
- Barthelmie, R. J., and S. C. Pryor, 2013: An overview of data for wake model evaluation in the Virtual Wakes Laboratory. *Appl. Energy*, **104**, 834–844.
- , —, and S. T. Frandsen, 2009: Climatological and meteorological aspects of predicting offshore wind energy. *Offshore Wind Power*, J. Twidell and G. Gaudiosi, Eds., Multi-Science Publishing Co. Ltd., 43–69.
- , and Coauthors, 2010: Quantifying the impact of wind turbine wakes on power output at offshore wind farms. *J. Atmos. Oceanic Technol.*, **27**, 1302–1317.
- , K. S. Hansen, and S. C. Pryor, 2013: Meteorological controls on wind turbine wakes. *Proc. IEEE*, **101**, 1010–1019.
- Choukulkar, A., R. Calhoun, B. Billings, and J. Doyle, 2012: A modified optimal interpolation technique for vector retrieval for coherent Doppler lidar. *IEEE Geosci. Remote Sens. Lett.*, **9**, 1132–1136.

- Clive, P. J. M., 2012: Unlocking the value of lidar. *Proc. European Wind Energy Conf.*, Copenhagen, Denmark, EWEA, 1–9.
- Fitch, A. C., J. B. Olson, J. K. Lundquist, J. Dudhia, A. K. Gupta, J. Michalakes, and I. Barstad, 2012: Local and mesoscale impacts of wind farms as parameterized in a mesoscale NWP model. *Mon. Wea. Rev.*, **140**, 3017–3038.
- Gottschall, J., M. S. Courtney, R. Wagner, H. E. Jørgensen, and I. Antoniou, 2012: Lidar profilers in the context of wind energy—A verification procedure for traceable measurements. *Wind Energy*, **15**, 147–159.
- Hirth, B. D., J. L. Schroeder, W. S. Gunter, and J. G. Guynes, 2012: Measuring a utility-scale turbine wake using the TTUKa mobile research radars. *J. Atmos. Oceanic Technol.*, **29**, 765–771.
- Högström, U., 1988: Non-dimensional wind and temperature profiles in the atmospheric surface layer: A re-evaluation. *Bound.-Layer Meteor.*, **42**, 55–79.
- Iungo, G. V., Y. T. Wu, and F. Porté-Agel, 2013: Field measurements of wind turbine wakes with lidar. *J. Atmos. Oceanic Technol.*, **30**, 274–287.
- Kocer, G., G. Kocer, M. Mansour, N. Chokani, R. S. Abhari, and M. Muller, 2011: Full-scale wind turbine near-wake measurements using an instrumented uninhabited aerial vehicle. *J. Sol. Energy Eng.*, **133**, doi:10.1115/1.4004707.
- Koch, G. J., J. Y. Beyon, E. A. Modlin, P. J. Petzar, S. Woll, M. Petros, J. Yu, and M. J. Kavaya, 2012: Side-scan Doppler lidar for offshore wind energy applications. *J. Appl. Remote Sens.*, **6**, 063562, doi:10.1117/1.JRS.6.063562.
- Krishnamurthy, R., A. Choukulkar, R. Calhoun, J. Fine, A. Oliver, and K. S. Barr, 2012: Coherent Doppler lidar for wind farm characterization. *Wind Energy*, **16**, 189–206, doi:10.1002/we.539.
- Lange, M., and U. Focken, 2006: *Physical Approach to Short-Term Wind Power Prediction*. Springer-Verlag, 208 pp.
- Lenschow, D. H., 1986: Aircraft measurements in the atmospheric boundary layer. *Probing the Atmospheric Boundary Layer*, D. H. Lenschow, Ed., American Meteorological Society, 39–55.
- Mann, J., and Coauthors, 2009: Comparison of 3D turbulence measurements using three staring wind lidars and a sonic anemometer. *Meteor. Z.*, **18**, 135–140.
- Matejka, T., and R. C. Srivastava, 1991: An improved version of the extended velocity-azimuth display analysis of single-Doppler radar data. *J. Atmos. Oceanic Technol.*, **8**, 453–466.
- Newsom, R. K., L. K. Berg, W. J. Shaw, and M. L. Fischer, 2012: Dual-Doppler lidar for measurement of wind turbine inflow-outflow and wake effects. *Proc. 50th AIAA Aerospace Sciences Meeting including the New Horizons Forum and Aerospace Exposition*, AIAA 2012-0655, Nashville, Tennessee, AIAA, 9574–9590.
- Pichugina, Y. L., R. M. Banta, N. D. Kelley, B. J. Jonkman, S. C. Tucker, R. K. Newsom, and W. A. Brewer, 2008: Horizontal-velocity and variance measurements in the stable boundary layer using Doppler lidar: Sensitivity to averaging procedures. *J. Atmos. Oceanic Technol.*, **25**, 1307–1327.
- Rajewski, D. A., and Coauthors, 2013: Crop Wind Energy Experiment (CWEX): Observations of surface-layer, boundary-layer and mesoscale interactions with a wind farm. *Bull. Amer. Meteor. Soc.*, **94**, 655–672.
- Sanderse, B., S. P. van der Pijl, and B. Koren, 2011: Review of computational fluid dynamics for wind turbine wake aerodynamics. *Wind Energy*, **14**, 799–819.
- Sanz Rodrigo, J., F. Borbón Guillén, P. Gómez Arranz, M. S. Courtney, R. Wagner, and E. Dupont, 2013: Multi-site testing and evaluation of remote sensing instruments for wind energy applications. *Renewable Energy*, **53**, 200–210.
- Sathe, A., and J. Mann, 2012: Measurement of turbulence spectra using scanning pulsed wind lidars. *J. Geophys. Res.*, **117** (D1), D01201.
- , —, J. Gottschall, and M. S. Courtney, 2011: Can wind lidars measure turbulence? *J. Atmos. Oceanic Technol.*, **28**, 853–868.
- Shimada, S., T. Ohsawa, S. Chikaoka, and K. Kozai, 2011: Accuracy of the wind speed profile in the lower PBL as simulated by the WRF model. *SOLA*, **7**, 109–112.
- Skamarock, W. C., and J. B. Klemp, 2008: A time-split nonhydrostatic atmospheric model for weather research and forecasting applications. *J. Comput. Phys.*, **227**, 3465–3485.
- Smith, D., M. Harris, A. Coffey, T. Mikkelsen, H. Jørgensen, J. Mann, and R. Danielian, 2006: Wind lidar evaluation at the Danish wind test site in Høvsøre. *Wind Energy*, **9**, 87–93.
- Storm, B., J. Dudhia, S. Basu, A. Swift, and I. Giammanco, 2009: Evaluation of the Weather Research and Forecasting model on forecasting low-level jets: Implications for wind energy. *Wind Energy*, **12**, 81–90.
- Stull, R. B., 1988: *An Introduction to Boundary Layer Meteorology*. Kluwer, 666 pp.
- Suselj, K., and A. Sood, 2010: Improving the Mellor–Yamada–Janjic parameterization for wind conditions in the marine planetary boundary layer. *Bound.-Layer Meteor.*, **136**, 301–324.
- Wagner, R., M. Courtney, J. Gottschall, and P. Lindelow-Marsden, 2011: Accounting for the speed shear in wind turbine power performance measurement. *Wind Energy*, **14**, 993–1004.